



Smart Nanosystem-Mediated Inhibition of Mitochondrial Respiration for Enhanced Phototherapy-Induced Antitumor Immunity

Yifan Zhao, Bai Lv, Guanghe Xue, Yong Sun , Jie Cao 

Department of Pharmaceutics, School of Pharmacy, Qingdao University, Qingdao, 266071, People's Republic of China

Correspondence: Jie Cao; Yong Sun, Email caojie0829@hotmail.com; sunyong@qdu.edu.cn

Introduction: Here, based on oxygen-dependent photodynamic therapy (PDT) and oxygen-consumed oxidative phosphorylation of cancer tissues, we designed and developed a nanosystem (named CyI&Met-Liposome, LCM) to co-encapsulate the photosensitizer CyI and mitochondrial respiration inhibitor metformin (Met) as a PDT enhancer.

Methods: We synthesized nanoliposomes encapsulating Met and CyI with excellent photodynamic/photothermal and anti-tumor immune properties using a thin film dispersion method. Confocal microscopy and flow cytometry were used to assess the cellular uptake, PDT, photothermal therapy (PTT) and immunogenicity of nanosystem in vitro. Finally, two tumor models in mice were constructed to investigate the tumor suppression and immunity in vivo.

Results: The resulting nanosystem relieved hypoxia in tumor tissues, enhanced PDT efficiency, and amplified antitumor immunity induced by phototherapy. As a photosensitizer, CyI effectively killed the tumor by generating toxic singlet reactive oxygen species (ROS), while the addition of Met reduced oxygen consumption in tumor tissues, thereby evoking an immune response via oxygen-boosted PDT. Both in vitro and in vivo results illustrated that LCM effectively restricted the respiration of tumor cells to reduce tumor hypoxia, thus providing continuous oxygen for enhanced CyI-mediated PDT. Furthermore, T cells were recruited and activated at high levels, providing a promising platform to eliminate the primary tumors and synchronously realize effective inhibition of distant tumors.

Keywords: photodynamic therapy, immunogenic cell death, oxidative phosphorylation, tumor immunotherapy

Introduction

At present, photodynamic therapy (PDT) is one of the most promising tumor treatment methods. Compared with radiotherapy and chemotherapy with systemic toxicity, PDT has been widely reported to be used in tumor treatment because of its advantages of low invasiveness, minimal side effects, short treatment period and high selectivity.¹

PDT utilizes photosensitizers (PSs) to convert oxygen to cytotoxic reactive oxygen species (ROS), especially singlet oxygen (1O_2), which leads to cytotoxicity and vascular damage, resulting in tumor cell death.² In recent years, we have realized that a more important phenomenon caused by phototherapy is immunogenic cell death (ICD), which releases damaged-associated molecular patterns (DAMPs), thus increasing the immunogenicity of the tumor microenvironment.³⁻⁶

ICD is a regulatory cell death mode, which activates innate and adaptive immune responses by coordinating the complex information transmission between dead tumor cells and immune cells.⁷ Following the induction of ICD, dying tumor cells release specific biomolecule messenger DAMPs, such as calreticulin (CALR), and heat shock protein 70 (HSP70), which stimulate the immune response. Exposure of CALR on the plasma membrane during the early stage of ICD serves as an important “eat me” signal, which is recognized by CD91 receptors on phagocytes, leading to tumor cell uptake and cross presentation of tumor antigens to tumor-specific cytotoxic T cells. HSP70 plays an important role in the cross presentation of tumor antigen peptides on major histocompatibility complex (MHC) class I molecules, which in turn activate tumor-specific T lymphocytes.⁸⁻¹⁰

The main issue surrounding the use of PDT as an inducer of ICD lies in the limitation of oxygen. On the one hand, the hypoxic characteristics of the tumor microenvironment restrict the utilization of O₂ by PDT; on the other hand, the efficacy of PDT will further aggravate hypoxia. Compared to common external oxygen supplement strategies such as perfluorocarbon,¹¹ and hemoglobin,¹² PDT, regardless of the underlying mechanism, can only temporarily relieve hypoxia, but tumor recurrence may occur. Oxidative phosphorylation plays an important role in numerous cancers, not only by providing material energy for tumor growth but also by promoting the occurrence and development of tumors.^{13–15} More importantly, oxidative phosphorylation occurs at the cost of oxygen consumption.^{16,17} Therefore, inhibiting oxidative phosphorylation may reduce the respiratory oxygen consumption of tumor cells, and compared to directly delivering oxygen, reducing the oxygen consumption of cells is a more effective means of improving tissue hypoxia. Metformin (Met) has been found to significantly inhibit oxidative phosphorylation by inhibiting complex I in the oxidative phosphorylation pathway.¹⁸ Given this, we imagine that it can be used as an oxidative phosphorylation inhibitor to destroy the electronic respiratory chain by inhibiting complex I, thus reducing the consumption of endogenous oxygen.

Here, we designed and developed a nanosystem that not only relieves tumor hypoxia and reduces hypoxia-induced PDT resistance but also enhances phototherapy-induced antitumor immunity. We have previously synthesized a non-toxic iodized derivative of cyanine dye, CyI, which has been demonstrated to enhance ¹O₂ production, with good photothermal conversion and near-infrared imaging function.¹⁹ Therefore, we selected CyI as a PS and Met as a PDT enhancer and encapsulated them in liposomes to construct a nanosystem to magnify the antitumor effect of PDT and enhance the phototherapy-induced antitumor immunity (Figure 1A). Met inhibits the endogenous oxygen consumption of tumors and supplies more oxygen to the photosensitizer CyI. Then, CyI produces ROS in the presence of oxygen, which leads to apoptosis and necrosis of tumor cells. Meanwhile, CyI can induce an acute inflammatory response in the tumor microenvironment, stimulate cells to release secondary inflammatory mediators, induce CALR exposure, release tumor-associated antigens (TAAs), stimulate the maturation and activation of DCs, and increase immunogenicity. Briefly, the tumor itself becomes an antigen, which stimulates the innate immune pattern recognition receptors (PRRs) or other activated receptors on antigen-presenting cells (APCs), induces ICD, enhances antigen presentation, activates T cells or memory T cells to activate immune cells, and ultimately, stimulates a systemic antitumor immune response.

Materials and Methods

Materials

NIR dye CyI (MW 776.5) was prepared in our laboratory. Egg yolk lecithin (PC-98T) was acquired from AVT Pharmaceutical Tech Co. (Shanghai, China). 1,2-distearoyl-sn-glycero-3-phosphoethanolamine-N-[methoxy(polyethylene glycol)-2000] (DSPE-PEG₂₀₀₀) was purchased from Ruixi Bio-tech Co. (Xi'an, China). Metformin was purchased from Macklin. Singlet Oxygen Sensor Green (SOSG) was purchased from Meilunbio. DAPI solution, Methyl thiazolyl-tetrazolium (MTT), Annexin V-FITC/PI apoptosis staining kit were purchased from Solarbio (Beijing, China).

Mouse colon cancer cells (CT26) were purchased from Wuhan Procell Life Science & Technology Co. Ltd. (Wuhan, China). Cells were cultured in Roswell Park Memorial Institute-1640 (RPMI-1640, Procell, USA) with 10% fetal bovine serum (Procell, USA) and 1% penicillin-streptomycin (Hyclone, USA). BALB/c mice were purchased from Beijing Vital River Laboratory Animal Technology Co., Ltd. (Beijing, China).

Preparation of LCM

The liposomes encapsulating CyI and Met were synthesized by a thin-film hydration method. Briefly, egg yolk lecithin, cholesterol, distearoyl phosphoethanolamine-PEG₂₀₀₀ (DSPE-PEG₂₀₀₀), and CyI were dissolved in chloroform at specific concentrations, before removing the organic solvent. Next, PBS containing Met was added to dissolve the film under vortexing for 1 h at 60°C. Finally, the un-encapsulated CyI and Met were removed by filtering through a 220 nm nitrocellulose membrane.

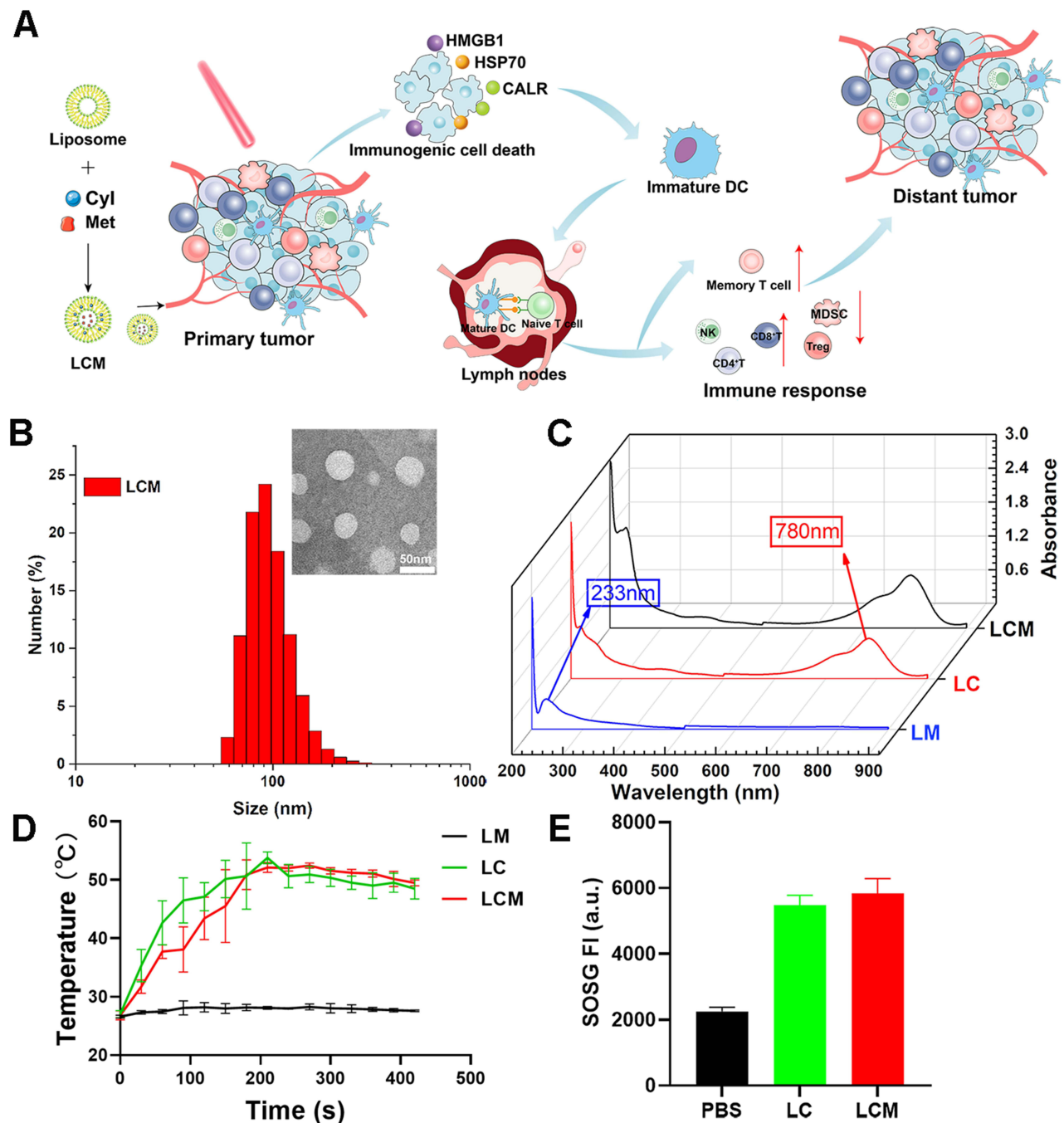


Figure 1 (A) Schematic illustration of the nanosystem (named as Cyl&Met-Liposome) used to provide NIR-induced phototherapy immunotherapy as a cancer treatment. (B) Transmission electron microscopy (TEM) images and size distribution of LCM. (C) UV-Vis-NIR absorption of LM, LC, and LCM. (D) Temperature change curves of LM, LC, and LCM exposed to NIR irradiation (808 nm, 0.96 W/cm²). (E) Singlet oxygen (¹O₂) production by PBS, LC, and LCM under 808 nm, 0.96 W/cm² NIR irradiation.

Measurement of in vitro Photodynamic and Photothermal Effects

In vitro ¹O₂ Detection

The detection of ¹O₂ in vitro was evaluated by SOSG, which has a maximum excitation wavelength of 504 nm and an emission wavelength of 525 nm. Briefly, Cyl, LC, LCM, and PBS solutions with the equivalent concentration of Cyl (120 μg/mL) were mixed with SOSG (25 μM) and irradiated by NIR irradiation (808 nm, 0.96 W/cm²) for 5 min. The samples were analyzed with a Tecan Infinite 200pro.

Detection of Cellular ROS

The intracellular photodynamic effect was detected by using a confocal laser scanning microscope (CLSM) with the DCFH-DA fluorescent probe as the sensor. First, CT26 cells were cultured in confocal dishes for 24 h, followed by LCM culture for 6 h in normoxic and hypoxic conditions. Subsequently, the cells were washed with PBS and incubated with DCFH-DA (10 μM). After 20 min, the cells were irradiated with NIR (808 nm, 0.96 mW cm^{-2}) for 3 min, with ROSUP (an ROS inducer) as the positive control group. Finally, the intracellular fluorescence was observed by using the CLSM to evaluate the production of ROS.

Detection of Photothermal Effect

The photothermal effect of LCM or LC was evaluated by recording the temperature curve of the sample irradiated with NIR at 808 nm, 0.96 W/cm^2 . The temperature was quantified using a thermocouple thermometer (TES Electrical Electronic Corp, WRNK-104) at designated time intervals.

Cellular Uptake

Cellular uptake was studied by using a CLSM and via flow cytometry. In brief, CT26 cells were seeded and cultured for 24 h. Subsequently, the cells were treated with LCM (120 $\mu\text{g/mL}$) for 2, 4, 6, and 8 h, then stained with DAPI, and finally observed with the CLSM. Meanwhile, the cells were collected by digestion and centrifugation and then analyzed by flow cytometry.

MTT Assay

First, CT26 cells were seeded in 96-well microtiter plates and cultured for 24 h. Then, the cells were incubated with gradient concentrations of LC or LCM under normoxic and hypoxic conditions. After 6 h, the cells were irradiated with NIR light (808 nm, 0.96 mW cm^{-2}) for 5 min. After incubation for another 24 h, MTT (5 mg/mL) was added to each well and incubated for 4 h. Subsequently, the culture medium in each well was replaced by DMSO. Finally, the absorbance of DMSO solution was measured using a microplate reader at 570 nm.

In vitro Examination of ICD

To determine the induction of ICD, the surface expression of CALR, as well as the release of HSP70, were studied in vitro. Briefly, CT26 cells were incubated with LCM or LC, irradiated for 3 min, and then cultured for 24 h. Subsequently, antibodies to CALR, and HSP70 were added and incubated at room temperature without light for 2 h. Following incubation, the secondary antibody labeled with Alexa Fluor 647 was added and incubated for 1 h at room temperature. Finally, the fluorescence changes were observed by using a CLSM.

In vivo Evaluation of PDT/PTT Efficacy

Evaluation of Tumor Growth Inhibition

BALB/c mice bearing tumors were randomly divided into four groups. Each group of mice was intravenously injected with different solutions (200 μL) using the following treatment regimens: (A) Saline without laser irradiation (control group); (B) Saline with laser irradiation (808 nm, 0.96 W/cm^2 , 5 min, NIR group); (C) LC under NIR irradiation (0.96 W/cm^2 , 5 min, 1.5 mg/kg , LC group); and (D) LCM under NIR irradiation (0.96 W/cm^2 , 5 min, 1.5 mg/kg , LCM group). The tumor volume and body weight of the mice in each group were recorded daily. After 15 days of treatment, tumors and main organs were collected for histological analysis with H&E, Ki67, and TUNEL staining.

Evaluation of PDT Efficacy

Intratumoral $^1\text{O}_2$ generation was evaluated by using SOSG. Briefly, 200 μL saline, LC, or LCM was mixed with 50 μL SOSG (25 μM), and then injected into the tail vein of tumor-bearing mice. Then, the tumors were exposed to NIR light (808 nm, 0.96 W/cm^2 , 5 min). After 6 h, the tumors were isolated from each mouse for confocal imaging.

Analysis of Immune Cell Populations in Tumors

The tumor tissues of each group were digested with collagenase to prepare a tumor single cell suspension, and the double positive markers of CD11c and MHCII were detected after flow antibody staining. In parallel, the tumors were stained with CALR, HMGB1, CD86, CD11c, and MHCII, and CD4⁺T, CD8⁺T, MDSCs, memory T cells, NK cells, Tregs, and M2 macrophages in the tumor tissue suspension were detected by flow cytometry.

Statistical Analysis

Data are presented as the mean \pm SD. Statistical analysis was performed using Students' *t*-test, with $P < 0.05$ indicating statistical significance.

Results and Discussion

Synthesis and Characterization

CyI, an iodinated cyanine dye, was used as the photosensitizer, and Met, an inhibitor of mitochondrial oxidative phosphorylation, was prepared by thin film hydration method to construct the nanosystems. DSPE-PEG2000 was used to improve liposome stability. As illustrated in [Figure 1B](#), transmission electron microscopy (TEM) images showed that the nanosystem was monodisperse, with a uniform particle size distribution. Dynamic light scattering (DLS) measurements further demonstrated that the size of the liposome-CyI-Met (LCM) was 99.8 ± 1.4 nm, with an average hydrodynamic size (poly dispersion index: 0.15 ± 0.05) and good stability in plasma, allowing the LCM to penetrate deeper tumor areas through enhanced permeability and retention effect (EPR). Moreover, the potential of the LCM was -9.19 ± 0.31 mV. Additionally, the UV-vis absorption spectra of the liposome-CyI (LC), liposome-Met (LM), and LCM showed that the characteristic absorption peaks of CyI (780 nm) and Met (233 nm) were observed in the LCM, indicating that the drugs were encapsulated in the nanosystem ([Figure 1C](#)). Furthermore, the drug encapsulation efficiency (EE%) of Met and CyI was 31.92% and 54.94%, respectively, while the drug loading efficiency (LE%) of Met and CyI was 3.67% and 5.34%, respectively.

We previously confirmed that CyI can generate photodynamic and photothermal effects under irradiation at 808 nm, 0.96 W/cm^2 .¹⁹ Therefore, we next measured the ability of the LCM to produce ¹O₂ and heat in vitro in response to NIR irradiation to examine its photothermal effects. Blank liposome, LC, LM, and LCM were exposed to 808 nm, 0.96 W/cm^2 NIR irradiation to monitor and record the temperature changes during exposure. As shown in [Figures 1D](#) and [Figure S1](#), neither the blank liposomes nor the LM showed obvious temperature changes during the illumination period. In contrast, the temperature of the LC and LCM increased rapidly under laser illumination and reached a plateau within 5 min, with the highest temperatures recorded as 54.2°C and 53.8°C, respectively. These results demonstrate that both LC and LCM have good photothermal efficiency under 808 nm, 0.96 W/cm^2 NIR irradiation. We then used singlet oxygen sensor green (SOSG) as a fluorescent probe to examine the ability of the LCM to induce photodynamic effects. As illustrated in [Figure 1E](#), the fluorescence intensity of the LCM was similar to that of the LC and was significantly higher than that of the PBS group (control group) after laser irradiation (808 nm, 0.96 W/cm^2) for 5 min. The results showed that both LCM and LC produced large amounts of ¹O₂. Therefore, our results demonstrate that the nanosystem can efficiently generate heat and ¹O₂ under NIR irradiation, indicating the potential of the LCM in combination with PDT and photothermal therapy (PTT) for effective cancer therapy.

In vitro Inhibition of Cell Respiration to Reduce Oxygen Consumption

After confirming that the LCM showed the photodynamic and photothermal properties of CyI, we studied the mitochondrial respiratory inhibition of Met. It has been reported that the disturbance of electron transfer in the electron respiratory transport chain leads to mitochondrial dysfunction, which is characterized by the change in mitochondrial membrane potential ($\Delta\Psi_m$).^{20,21} Therefore, we used JC-1 to explore whether LCM can reduce cell oxygen consumption by inhibiting electron transport in the respiratory chain, resulting in abnormal $\Delta\Psi_m$. The membrane potential of normal healthy mitochondria is polar, which rapidly accumulates JC-1 in the mitochondria and forms aggregates with red fluorescence. In contrast, when the $\Delta\Psi_m$ is destroyed, JC-1 is released from the mitochondria and emits green

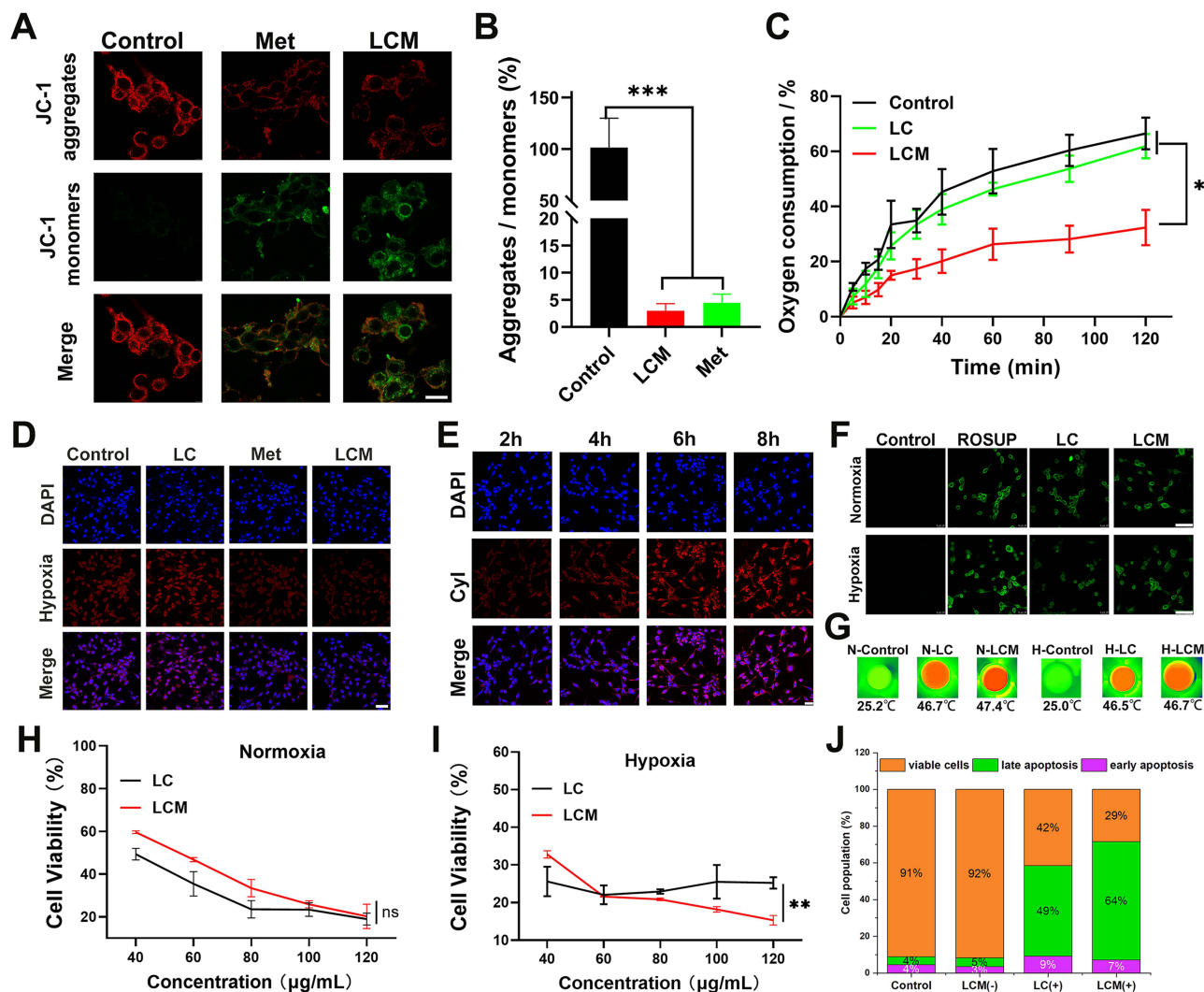


Figure 2 (A) CLSM showing the mitochondrial membrane potential of CT26 cells in response to different treatments. Scale bar: 40 μm . (B) Rate of JC-1 aggregates to JC-1 monomers. (C) Determination of CT26 cell oxygen consumption by measurement of DO content 6 h after administration without laser irradiation. (D) Representative fluorescent images of the hypoxia probe in CT26 cells after different LCM. Scale bar: 50 μm . (E) Confocal fluorescence images of CT26 cells cultured with LCM for various times. Scale bar: 25 μm . (F) Confocal fluorescence images of ROS generation in CT26 cells incubated with LC and LCM. Scale bar: 50 μm . (G) Thermal images of CT26 cells under conditions of normoxia (H) and hypoxia (I), as measured by MTT assay, ns: no significant difference. (J) Apoptosis and histogram distribution of quantitative results detected by flow cytometry after various treatments under hypoxic conditions. ns>0.05, *P<0.05, **P<0.01, ***P<0.001.

fluorescence in the cytoplasm in the form of monomers. As shown in Figure 2A and B, the control group showed strong red fluorescence, indicating that the $\Delta\Psi\text{m}$ was higher and that the mitochondria were in a normal state. In contrast, cells co-incubated with Met and LCM showed strong green fluorescence, indicating a decrease in the $\Delta\Psi\text{m}$, whereby the $\Delta\Psi\text{m}$ was depolarized and the respiration of cells was affected. The result showed that the mitochondrial membrane was depolarized after LCM treatment, which indicated that LCM caused mitochondrial dysfunction.

Next, we evaluated the respiratory inhibition ability of Met by measuring the cell oxygen consumption rate (OCR%), an important indicator of cell mitochondrial activity and oxidative phosphorylation.²² Tumor cells have exuberant metabolism and are high consumers of oxygen, which is also one of the causes of hypoxia at the tumor site. As illustrated in Figure 2C, we used a JPB-607A-dissolved oxygen meter to determine the content of dissolved oxygen in closed cell solution. In the CT26 cell untreated group (control group), the dissolved oxygen in the blocked solution decreased gradually, while the decrease in dissolved oxygen content in the Met group was inhibited. Additionally, Met inhibited the respiration of cells in a concentration-dependent manner; the increase in Met concentration from 0.1 mM to

2 mM resulted in an obvious decrease in dissolved oxygen content (Figure S2). Similar to the control group, the OCR% of the LC group increased gradually, while that of the LCM group decreased significantly in parallel. Therefore, we believe that Met inhibits the oxidative phosphorylation of CT26 cells, thus reducing the endogenous oxygen consumption.

Next, to prove that LCM can reduce the cellular oxygen partial pressure caused by cell respiration under hypoxic conditions, the anoxic state of cells was detected by immunofluorescence. As shown in Figure 2D, the control group showed hypoxia (red fluorescence), while the cells in the Met treatment group showed a weakening of red fluorescence. Moreover, compared to the LC treatment group, the hypoxia in the LCM treatment group showed a trend of weakening red fluorescence, indicating that Met can effectively reduce the hypoxic state of cells. These results demonstrate that LCM can alleviate oxygen consumption and reduce oxygen partial pressure by inhibiting cell respiration, which makes it possible to provide more oxygen to CyI to exert the effect of PDT.

Phototherapy Effects of LCM in vitro

Next, to investigate the cellular uptake efficiency of LCM by CT26 cells, the uptake behavior of CT26 cells was studied via CLSM and flow cytometry. After co-incubating for different time periods, the red fluorescence signal from CyI was observed in CT26 cells. As depicted in Figure 2E and Figure S3, when the cells were co-incubated with LCM for 6 h, the fluorescence intensity of CyI gradually increased, before stabilizing; therefore, we chose to use NIR for phototherapy after 6 h of incubation. These results show that LCM can be effectively absorbed by CT26 cells and used for further phototherapy and fluorescence imaging.

Inspired by the excellent properties of LCM, we then determined whether relieving hypoxia enhanced the production of ROS. We used a DCFH-DA detection kit to explore the ROS production ability of LCM under normoxic and hypoxic conditions. Interestingly, compared to the positive control group (ROSUP), LC and LCM produced similar and strong ROS fluorescence signals under normoxia, both of which were stronger than those of the ROSUP group. Under hypoxic condition, the Met in the LCM that inhibit oxygen consumption, which increases the production of ROS compared to LC (Figure 2F). The results of flow analysis are consistent with the fluorescence results, in that they show that the LCM has a superior ROS yield. These findings highlight that the effective reduction of cell oxygen consumption will greatly promote the production of ROS and enhance PDT during hypoxia (Figure S4). As depicted in Figure 2G and Figure S5, we then investigated the photothermal effect of LCM. The results demonstrate that the photothermal effect of LCM shows a consistent trend under both normoxic and hypoxic conditions, that is, with the extension of time, the temperature of the LCM gradually increases (the highest value is 46.7°C under hypoxia, which is higher than the 43°C required for efficient PTT²³). It is worth mentioning that we observed no significant difference between the LCM and LC; this may be because the efficacy of PTT does not depend on oxygen content, which results in the LCM and LC having similar photothermal effects.

To further prove that reducing oxygen consumption can enhance the PDT effect of hypoxia, CT26 cells were incubated with gradient concentrations of LC and LCM and detected by MTT assay. In the absence of NIR, the LCM showed no cytotoxicity under normoxic and hypoxic conditions, which indicated that the LCM could be safely used in phototherapy only under NIR irradiation (Figure S6). There was no significant difference in phototoxicity between LC and LCM under normoxic conditions (Figure 2H). In contrast, the survival rate of cells treated with LCM under hypoxia was significantly lower than that of the LC group, indicating that Met could assist CyI in phototherapy and induce cell death under hypoxia (Figure 2I). The CT26 cells were co-incubated with LCM during hypoxia, and the rate of apoptosis was detected by flow cytometry. Compared to the control group, when LCM was not exposed to NIR, the cell survival rate was 92%, and apoptosis was negligible, further confirming the safety of LCM. Because CyI released a large amount of ROS and heat to effectively kill tumor cells under NIR irradiation, the survival rate of LC and LCM cells was significantly decreased compared to that of the control group, at 42% and 29%, respectively. Furthermore, the apoptosis rate of CT26 cells treated with LCM was 71% in the early and late stages, which was more than the 58% observed in the LC group. These findings further confirm that Met increases PDT and induces cell damage and death during hypoxia (Figure 2J and Figure S7).

Phototherapy Induced Immune Activation of LCM in vitro

ICD is widely used in antitumor immunotherapy owing to its function in immune regulation, and it is frequently combined with phototherapy to maximize the antitumor immunotherapy effect. Recently, several DAMPs, including surface-exposed calreticulin (ecto-CALR), and HSP70, have been confirmed to play significant roles in ICD. To demonstrate whether the novel nanosystem can promote the ICD, we measured the exposure and release of specific DAMPs after different treatments.

Exposure of CALR on the surface of cancer cells functions to induce strong phagocytosis, promoting the uptake of dying or dead cells by APCs,²⁴ especially DCs, which then migrate to lymph nodes and present antigens to immature CD8⁺ T cells. Therefore, we first examined ecto-CALR by CLSM. The results showed that compared to the control and LCM groups without NIR irradiation, CALR was significantly expressed in the LC and LCM groups after irradiation. Moreover, the semi-quantitative fluorescent results demonstrated that the fluorescence of the LCM+L group was significantly stronger than that of the LC+L group, which indicated that CyI could effectively stimulate CALR exposure by phototherapy under laser irradiation, and the effect was significantly increased under the action of Met (Figure 3Ai and Aii).

The high expression of HSP under stress is another important signal that mediates the immunogenic death of tumor cells. In the early stage of ICD, HSP70 carries the tumor antigen peptide and is exposed on the cell surface in the form of a high-immunogenicity complex. HSP70 can also promote the secretion of pro-inflammatory factors such as IL-1 β , IL-12, and IL-6 in DCs and further enhance the immune response.¹⁰ Compared to the control and LCM groups without NIR

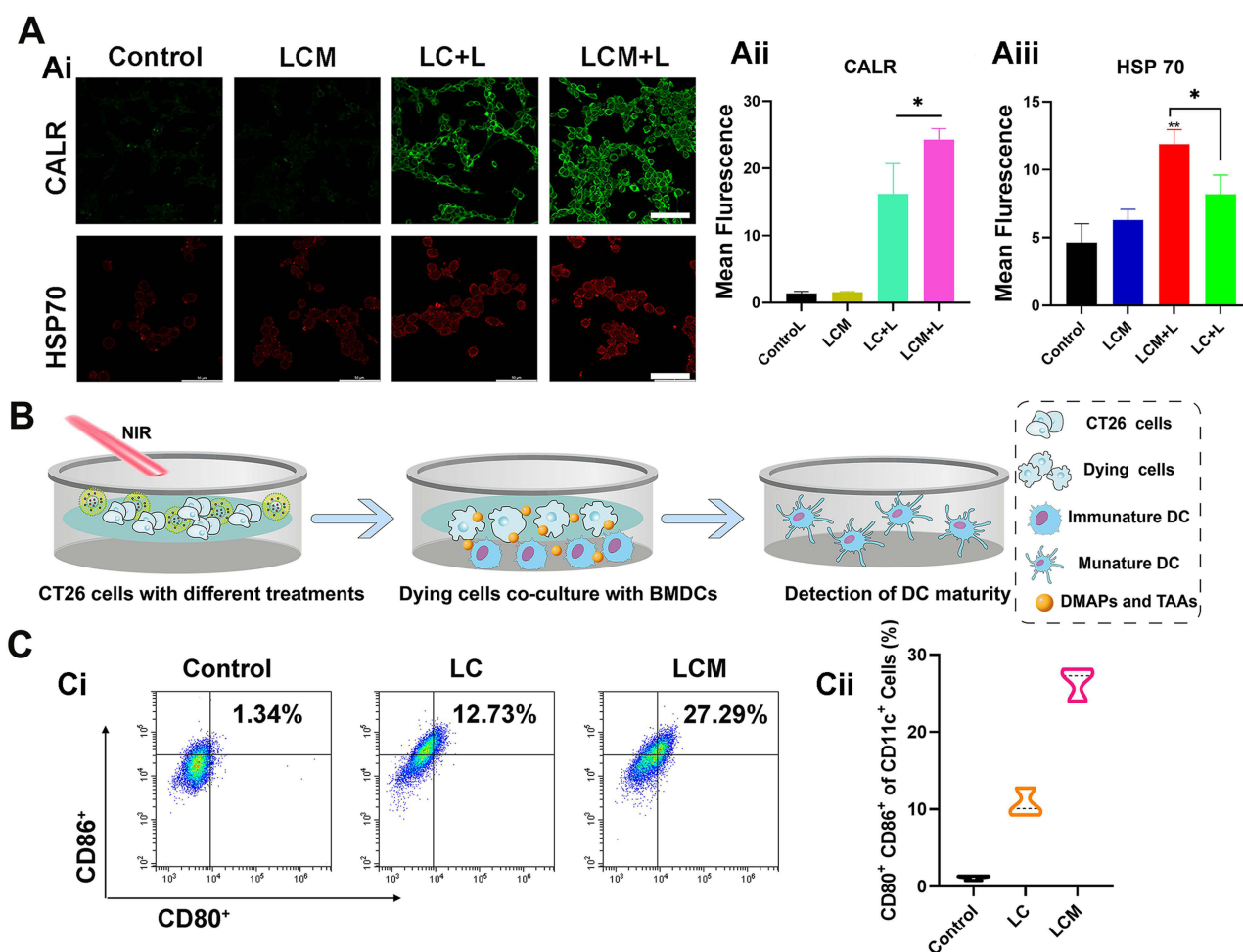


Figure 3 (A) CLSM images (Ai) and mean fluorescence intensity analysis of surface-exposed CALR (Aii) and HSP70 (Aiii) on CT26 cells after different treatments. Scale bar: 50 μ m. (B) Schematic diagram of the experimental design of the in vitro CT26 cell-BMDC co-culture assay using a Transwell system. (C) Representative flow cytometric plots (Ci) and quantitative analysis of mature DCs (Cii) following various treatments (n = 3). **p* < 0.05.

irradiation, the LC+L and LCM+L groups showed stronger fluorescence intensity (Figure 3Ai), demonstrating that both LC and LCM can induce the release of HSP70 under NIR. Moreover, the semi-quantitative results demonstrate that the LCM+L group induced the highest level of HSP release (Figure 3Aiii). To summarize, we consider that LCM-mediated PDT is conducive to the induction of ICD, thereby playing an indispensable role in killing primary tumors.

DAMPs released by dying cancer cells as a “danger signal” of the immune system induce DC maturation and activate the antitumor immune response mediated by T cells. Therefore, we next tested whether LCM-induced ICD could effectively promote the maturation of DCs. In addition to the antigen phagocytosis and presentation function, DCs also possess co-stimulatory molecules (CD80/CD86). By binding to the CD28 receptor of initial T cells, the B7-1 (CD80) and B7-2 (CD86) proteins on APCs provide the necessary co-stimulatory signals to promote the activation, proliferation, and differentiation of T cells. Therefore, to evaluate LCM-ICD-induced DC maturation, bone marrow-derived dendritic cells (BMDCs) were co-cultured with treated CT26 cells and then analyzed by flow cytometry. As illustrated in Figure 3B, CT26 cells were inoculated with LCM in the culture dish for 24 h, and co-cultured with immature BMDCs for 24 h after NIR irradiation. The mature state of CT26 cells was detected through flow cytometry. The results showed that the mature DC of the LCM group was about 27%, which was 2.5-fold higher than that of the LC group (Figure 3C).

Therefore, we conclude that the phototherapy of LCM under NIR could elicit CALR translocation to the cell surface and promote the release of HSP70, resulting in the induction of ICD response and DC maturation to evoke antitumor immunity.

In vivo LCM-Mediated Phototherapy

After comprehensive in vitro experiments, it was necessary to track the distribution of LCM in vivo to select the most appropriate laser irradiation time to maximize the therapeutic effect of PDT in vivo. Therefore, the in vivo fluorescence images were monitored after intravenous injection (i.v.). As depicted in Figure S8, after i.v. LCM, the tumor sites were gradually visible within 24 h due to the EPR effect, indicating efficient accumulation in tumors.

When the tumors grew to a volume of approximately 200–300 mm³, the tumor-bearing mice were randomly divided into four groups and numbered As shown in Figure 4A and B, compared to the saline and LC groups, the hypoxia probe

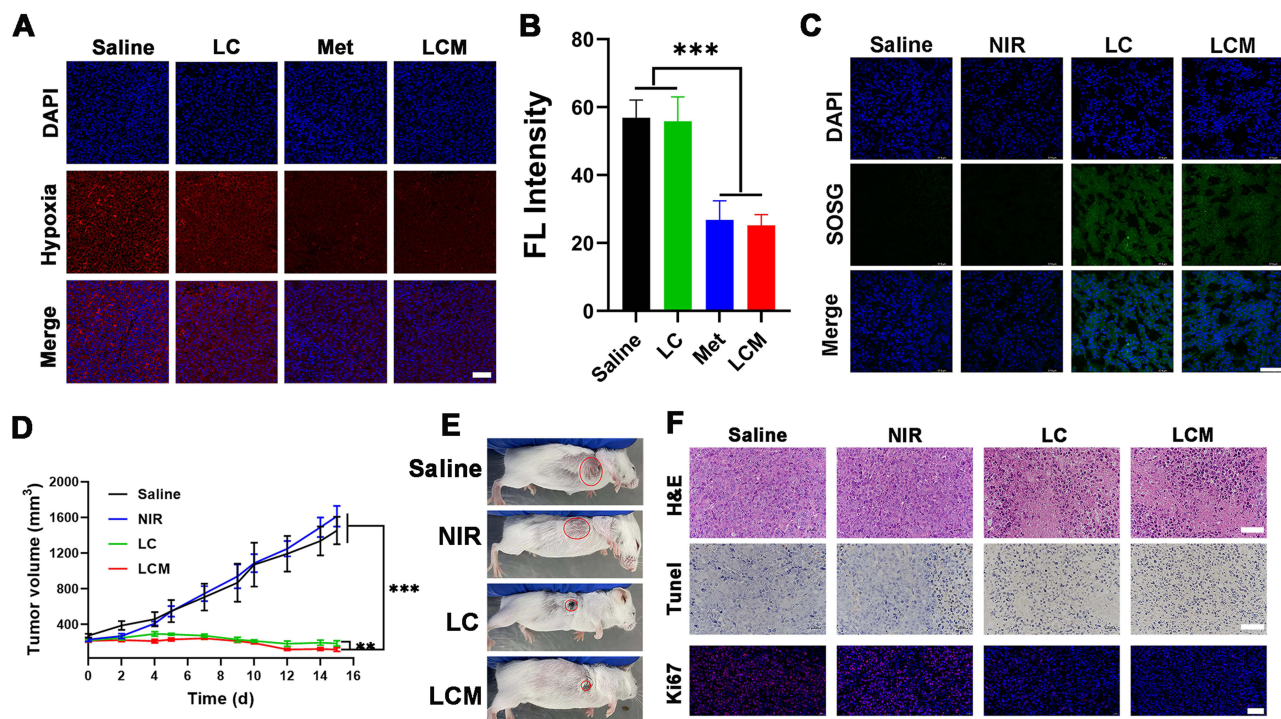


Figure 4 (A) Immunofluorescence images of tumor sections. Scale bar: 50 μ m. (B) Semiquantitative fluorescence intensity of hypoxic areas. (C) CLSM of SOSG-stained slices during different treatments. (D) Changes in tumor volume of mice following different treatments. (E) Photos of mice after treatments. (F) Images of tumors stained with H&E, TUNEL (scale bar: 25 μ m), and Ki67 from each group (scale bar: 20 μ m). ** p < 0.01, *** p < 0.001.

fluorescence signal in the Met and LCM groups was significantly weakened, indicating that Met effectively alleviates the hypoxic environment of the tumor.

Next, we conducted an *in vivo* therapeutic evaluation of LCM using the CT26 tumor model. The tumor-bearing mice were randomly divided into a saline group, an NIR group, an LC group, and an LCM group. When the tumor volume reached 200–300 mm³, the mice were injected intravenously (CyI 1.5 mg/kg), and after 24 h, the mice in the NIR, LC, and LCM groups were exposed to laser light for PDT and PTT. At the end of the treatment, phototherapy and immunological analysis were conducted. As shown in [Figure 4C](#), tumors treated with LC or LCM showed obvious green fluorescence compared to the control groups, implying that ¹O₂ production is facilitated by CyI. In the LC and LCM groups, the tumor temperature reached up to 47–48°C, which was sufficient for irreversible tumor ablation ([Figure S9](#)).

During the treatment, the tumor volume and body weight of the mice were monitored every 2 days. As expected, there was no discernible difference in tumor volume between the NIR group and the saline group, while a significant reduction in tumor volume was observed in all other treatments ([Figure 4D](#)). Additionally, the body weights of the LC and LCM group mice showed no discernible decreases during the treatment period, suggesting that the treatments had a high level of biosafety ([Figure S10](#)). Moreover, the H&E staining of the organs showed similar results. After 15 days of treatment, the tumor was extracted from a representative mouse from each group and photographed ([Figure 4E](#)). Next, histological analysis was performed by H&E, Ki67, and TUNEL staining ([Figure 4F](#)). Compared to the other groups, LCM caused the most tumor cell death, indicating that the phototherapy effect of LCM was greatly improved by the addition of Met. Furthermore, immunofluorescence analysis demonstrated that the tumor tissue treated with LCM exhibited the weakest Ki67 staining, indicating that LCM maximally inhibited the cell proliferation and promoted apoptosis. Moreover, the heart, liver, spleen, lung, and kidney of all mice were stained with H&E ([Figure S11](#)). The results showed no significant damage to the main organs of the treated mice, which can be attributed to the improved biocompatibility and low dark toxicity of LCM *in vivo*.

Taken together, this phototherapy-nanosystem strategy of LCM could significantly enhance the PDT efficiency and amplify the CyI-induced damage to tumors, with low systemic toxicity *in vivo*.

Phototherapy Sensitized Immunotherapy *in vivo*

We next evaluated *in vivo* LCM-induced ICD by immunofluorescence. As illustrated in [Figure 5A](#), in accordance with the *in vitro* experimental results, LCM-treated tumors had stronger CALR and HMGB1 expression. Moreover, immunofluorescence and flow cytometry demonstrated increases in DC activation markers (MHCII, CD103, and CD11C). As shown in [Figure 5A](#) and [Figure S12](#), mice in the LC and LCM groups showed significantly enhanced DCs maturation compared to that in the saline group, demonstrating that the phototherapy treatment could boost DCs maturation in the tumor. More importantly, the LCM group exhibited the highest cell maturation efficacy. These data show that the LCM has a superior ability to induce an immunogenic form of cancer cell death.

To elucidate the underlying mechanism of immune responses after different treatments, we investigated the proportions of CD8⁺ T and NK cells by flow cytometry. Tumor cells undergoing ICD release TAAs, which are engulfed by APCs and presented to cytotoxic CD8⁺ T lymphocytes to initiate a tumor response. As shown in [Figure 5B](#), phototherapy treatment resulted in a 2–3-fold increase in the proportion of CD8⁺ T cells in tumors compared to the saline group. Notably, the number of CD8⁺ T cells in tumors in the LCM group was the highest. The proportion of natural killer cells (NK cells), another type of cytotoxic lymphocyte crucial to the innate immune system,²⁵ increased by 1.4–2.8-fold in the tumors treated with LC or LCM ([Figure 5C](#)). Tregs inhibit the proliferation, metabolism, and killing functions of CD8⁺ T cells, and they induce tumor immune escape by inhibiting antitumor immune responses, thereby promoting tumor growth and proliferation.²⁶ Myeloid-derived suppressor cells (MDSCs) are inhibitory myeloid-derived cells, which can inhibit normal innate and adaptive functions of other immune cells by inducing a state of non-response or tolerance, rendering them unable to remove mutated precancerous cells and kill tumor cells.^{27,28} Therefore, we investigated the proportion of MDSCs and Tregs by flow cytometry. As expected, the population of CD4⁺FoxP3⁺ T cells (Tregs) in tumors of the LCM with the laser irradiation group reached 1.56%, which was lower than the 3.46% of the LC with the laser irradiation group and 6.35% of the saline group ([Figure 5D](#)). Concurrently, LC and LCM treatments significantly

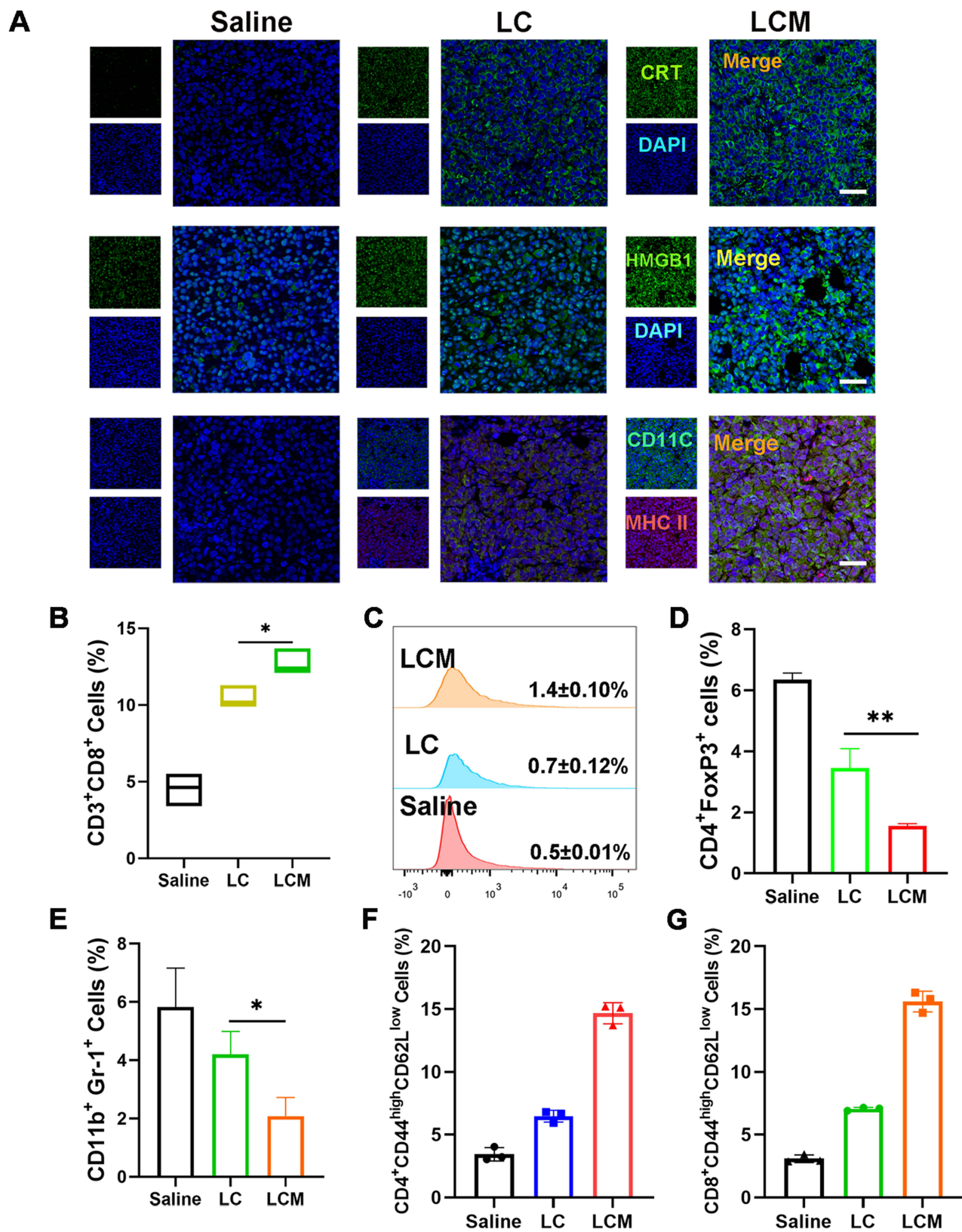


Figure 5 (A) Immunofluorescent imaging of CALR, HSP70, and DCs in mice after different treatments. Scale bar: 50 μm. Proportions of CD8⁺ cells (B), NK cells (C), Treg cells (D), MDSCs (E), and memory CD4⁺ (F) and memory CD8⁺ T cells (G) in tumors, n = 3, *p < 0.05, **p < 0.01.

decreased the MDSC population (Gr-1⁺ CD11b⁺) in tumors to approximately 28% and 64%, respectively, compared to the saline group (Figure 5E).

Memory T cells can identify specific microbes that have been encountered previously and can induce a rapid and robust response. We evaluated the proportion of memory CD4⁺ T cells and memory CD8⁺ T cells after treatment (identified as CD4⁺ CD44^{high} CD62L^{low} and CD8⁺ CD44^{high} CD62L^{low}, respectively). The results showed that LC group increased the proportion of memory CD4⁺ T cells by 1.88-fold and that of memory CD8⁺ T cells by 2.29-fold in the treated tumors, while LCM group increased the proportion of memory CD4⁺ T cells by 4.27-fold and that of memory CD8⁺ T cells by 5.06-fold in the treated tumors. Taken together, these data confirmed the high potency of LCM-mediated synergistic anti-cancer immunotherapy (Figure 5F–G).

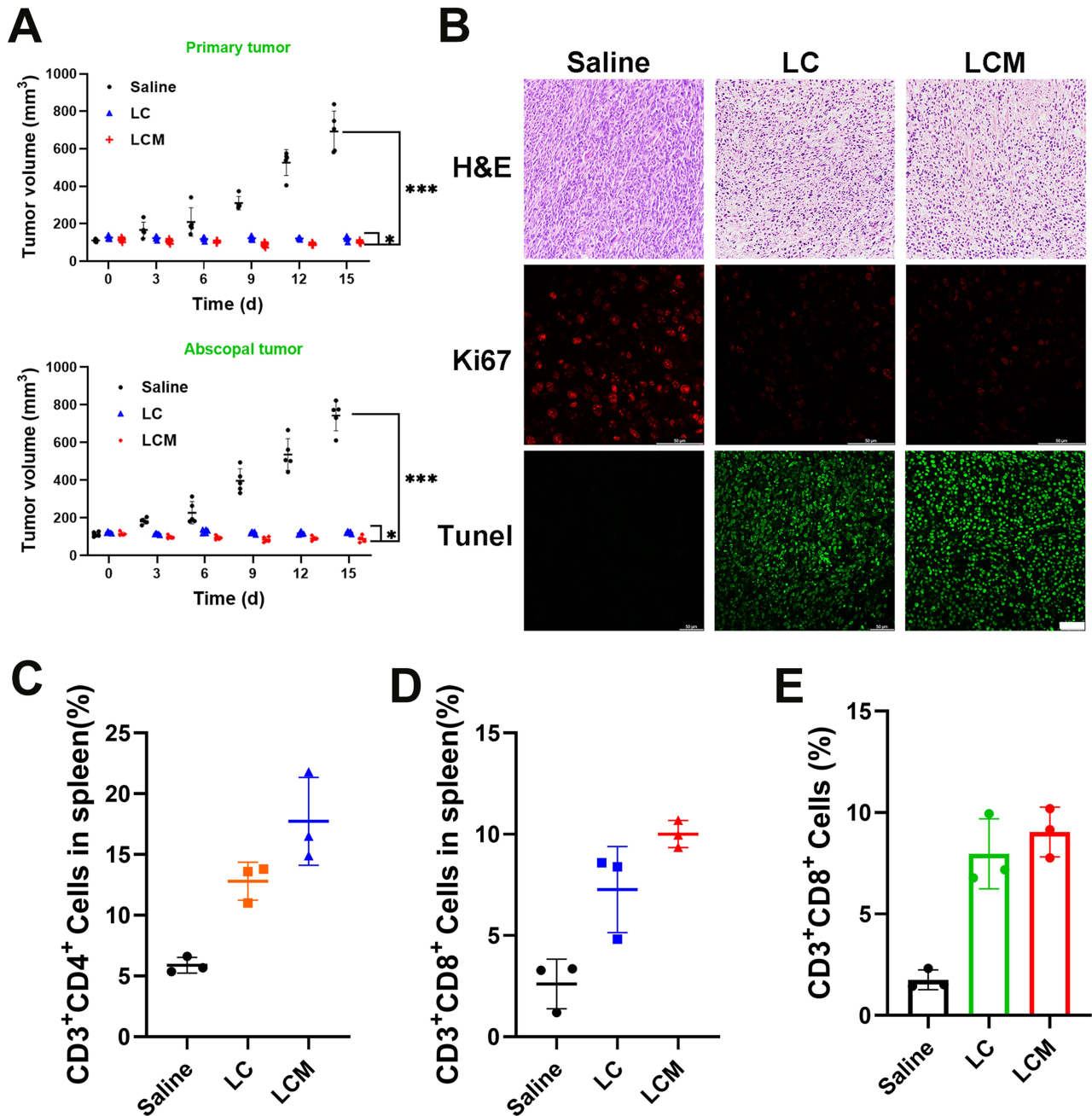


Figure 6 (A) Growth curves for the abscopal and primary tumors. (B) H&E, Ki67, and TUNEL staining of dual-tumor tissue slices from the saline, LC, and LCM groups (scale bar: 50 μm). CD4⁺ (C) and CD8⁺ (D) cells in the spleen and CD8⁺ T cells in distant tumors (E). *p < 0.05, ***p < 0.001.

The anticancer efficacy of LCM was then analyzed in a bilateral mouse tumor model. To this end, a bilateral mouse tumor model of colorectal cancer CT26 was developed by subcutaneously injecting cancer cells into both the left and right flank regions of BALB/c mice. The right tumors were designated as primary tumors for local NIR and the left tumors were designated as abscopal tumors with no direct treatment. When the primary and abscopal tumors reached 100–150 mm³, the mice were randomly divided into the following three groups (n = 4): Saline group, LC group, and LCM group (each group was exposed to radiation, followed by intratumoral injection). In comparison, the LCM with local NIR led to efficient tumor regression of the primary tumor, with tumors that measured 7.6% of the size of saline-treated tumors at the endpoint. More importantly, the tumor volume of abscopal tumors that did not receive local NIR was significantly controlled and tended to decrease after inoculation (Figure 6A). Histological analysis of abscopal tumors was performed using H&E staining, Ki67 staining, and TUNEL staining. As depicted in Figure 6B, no tissue damage or obvious cell proliferation was found in either type of tumor in the control group (the saline group). In contrast, obvious nuclear lysis and tumor necrosis were detectable in the tumors treated with LCM. Taken together, these results suggest that the novel nanosystem offers a strong antitumor immunological effect to inhibit the growth of tumor cells, even for cells without direct treatment.

As the LCM caused effective regression of both primary tumors and distant tumors in CT26 mouse models, which we hypothesized was due to effective systemic antitumor immune responses, we next investigated the antitumor immunity induced using flow cytometry. The spleen is the largest secondary lymphoid organ in the body, and it has a wide range of immune functions, largely owing to the high proportion of T and B cells in it.²⁹ Therefore, we collected the spleens to detect the expression of CD4 and CD8. As shown in Figure 6C and D, compared to the saline group, CD8⁺ T cells (CD3⁺ CD8⁺) in the LC and LCM treatment groups increased by 1.79% and 2.84% respectively, while CD4⁺ T cells (CD3⁺ CD4⁺) in the LC and LCM groups increased by 1.17% and 2.01%, respectively. Moreover, the proportion of CD8⁺ cells in abscopal tumors (Figure 6E) in the LC and LCM groups increased by 3.53% and 4.14%, respectively, compared to that of the saline group (1.76%).

Conclusion

In summary, LCM was tailor-made to function as a phototherapy-nanosystem nanoplatform. Met enabled the inhibition of mitochondrial respiration, which considerably economized intratumoral O₂ and further mitigated tumor hypoxia, providing more oxygen for CyI. The excellent phototherapy properties of CyI not only kill local tumors, induce inflammatory cell infiltration, and improve antitumor immune efficiency but also significantly inhibit the growth of abscopal tumors. The nanoplatform effectively modified the hypoxic tumor microenvironment (TME) to be conducive to the occurrence of ICD and immune cell infiltration, while the recruitment of immunosuppressive cells was significantly affected, thus greatly destroying the immunosuppressive function of the TME. As a result, the systemic immune response was significantly enhanced, resulting in ablation of the primary tumor and obvious control of tumor metastasis.

Animal Ethics Statement

BALB/c mice were provided by the Animal Experiment Center of Qingdao University. The study in vivo was performed under protocols approved by the Animal Management Rules of the Ministry of Health of the People's Republic of China (document No. 55, 2001) and the examination and approval of the Laboratory Animal Welfare Ethics Committee of Qingdao University (ethical approval number: 20221111BALB/c2820221204010).

Acknowledgments

This work was financially supported by National Natural Science Foundation of China (No. 32171362) and Natural Science Foundation of Shandong Province (No. ZR2022YQ73, ZR2021MH087).

Disclosure

The authors declare no conflicts of interest in this work.

References

1. Zhi D, Yang T, O'Hagan J, Zhang S, Donnelly RF. Photothermal therapy. *J Control Release*. 2020;325:52–71. doi:10.1016/j.jconrel.2020.06.032
2. Agostinis P, Berg K, Cengel KA, et al. Photodynamic therapy of cancer: an update. *CA Cancer J Clin*. 2011;61(4):250–281. doi:10.3322/caac.20114
3. Garg AD, Krysko DV, Vandenabeele P, Agostinis P. Hypericin-based photodynamic therapy induces surface exposure of damage-associated molecular patterns like HSP70 and calreticulin. *Cancer Immunol Immunother*. 2012;61(2):215–221. doi:10.1007/s00262-011-1184-2
4. Zhao LP, Zheng RR, Huang JQ, et al. Self-delivery photo-immune stimulators for photodynamic sensitized tumor immunotherapy. *ACS Nano*. 2020;14(12):17100–17113. doi:10.1021/acsnano.0c06765
5. Li W, Yang J, Luo L, et al. Targeting photodynamic and photothermal therapy to the endoplasmic reticulum enhances immunogenic cancer cell death. *Nat Commun*. 2019;10(1):3349. doi:10.1038/s41467-019-11269-8
6. Tian Y, Younis MR, Tang Y, et al. Dye-loaded mesoporous polydopamine nanoparticles for multimodal tumor theranostics with enhanced immunogenic cell death. *J Nanobiotechnology*. 2021;19(1):365. doi:10.1186/s12951-021-01109-7
7. Galluzzi L, Vitale I, Warren S, et al. Consensus guidelines for the definition, detection and interpretation of immunogenic cell death. *J Immunother Cancer*. 2020;8(1):e000337. doi:10.1136/jitc-2019-000337
8. Fucikova J, Kepp O, Kasikova L, et al. Detection of immunogenic cell death and its relevance for cancer therapy. *Cell Death Dis*. 2020;11(11):1013. doi:10.1038/s41419-020-03221-2
9. Krysko DV, Garg AD, Kaczmarek A, Krysko O, Agostinis P, Vandenabeele P. Immunogenic cell death and DAMPs in cancer therapy. *Nat Rev Cancer*. 2012;12(12):860–875. doi:10.1038/nrc3380
10. Tesniere A, Panaretakis T, Kepp O, et al. Molecular characteristics of immunogenic cancer cell death. *Cell Death Differ*. 2008;15(1):3–12. doi:10.1038/sj.cdd.4402269
11. Li Z, Zhu L, Sun H, et al. Fluorine assembly nanocluster breaks the shackles of immunosuppression to turn the cold tumor hot. *Proc Natl Acad Sci U S A*. 2020;117(52):32962–32969. doi:10.1073/pnas.2011297117
12. Jia Y, Duan L, Li J. Hemoglobin-based nanoarchitectonic assemblies as oxygen carriers. *Adv Mater*. 2016;28(6):1312–1318. doi:10.1002/adma.201502581
13. Evans KW, Yuca E, Scott SS, et al. Oxidative phosphorylation is a metabolic vulnerability in chemotherapy-resistant triple-negative breast cancer. *Cancer Res*. 2021;81(21):5572–5581. doi:10.1158/0008-5472.CAN-20-3242
14. Ding Y, Labitzky V, Legler K, et al. Molecular characteristics and tumorigenicity of ascites-derived tumor cells: mitochondrial oxidative phosphorylation as a novel therapy target in ovarian cancer. *Mol Oncol*. 2021;15(12):3578–3595. doi:10.1002/1878-0261.13028
15. Xue D, Xu Y, Kyani A, et al. Multiparameter optimization of oxidative phosphorylation inhibitors for the treatment of pancreatic cancer. *J Med Chem*. 2022;65(4):3404–3419. doi:10.1021/acs.jmedchem.1c01934
16. Molina JR, Sun Y, Protopopova M, et al. An inhibitor of oxidative phosphorylation exploits cancer vulnerability. *Nat Med*. 2018;24(7):1036–1046. doi:10.1038/s41591-018-0052-4
17. Xue D, Xu Y, Kyani A, et al. Discovery and lead optimization of benzene-1,4-disulfonamides as oxidative phosphorylation inhibitors. *J Med Chem*. 2022;65(1):343–368. doi:10.1021/acs.jmedchem.1c01509
18. Wheaton WW, Weinberg SE, Hamanaka RB, et al. Metformin inhibits mitochondrial complex I of cancer cells to reduce tumorigenesis. *Elife*. 2014;3:e02242. doi:10.7554/eLife.02242
19. Cao J, Chi J, Xia J, et al. Iodinated cyanine dyes for fast near-infrared-guided deep tissue synergistic phototherapy. *ACS Appl Mater Interfaces*. 2019;11(29):25720–25729. doi:10.1021/acscami.9b07694
20. El-Mir MY, Nogueira V, Fontaine E, Averet N, Rigoulet M, Leverve X. Dimethylbiguanide inhibits cell respiration via an indirect effect targeted on the respiratory chain complex I. *J Biol Chem*. 2000;275(1):223–228. doi:10.1074/jbc.275.1.223
21. Santos JH, Hunakova L, Chen Y, Bortner C, Van Houten B. Cell sorting experiments link persistent mitochondrial DNA damage with loss of mitochondrial membrane potential and apoptotic cell death. *J Biol Chem*. 2003;278(3):1728–1734. doi:10.1074/jbc.M208752200
22. Nolfi-Donagan D, Braganza A, Shiva S. Mitochondrial electron transport chain: oxidative phosphorylation, oxidant production, and methods of measurement. *Redox Biol*. 2020;37:101674. doi:10.1016/j.redox.2020.101674
23. Wu J, Li N, Yao Y, et al. DNA-stabilized silver nanoclusters for label-free fluorescence imaging of cell surface glycans and fluorescence guided photothermal therapy. *Anal Chem*. 2018;90(24):14368–14375. doi:10.1021/acs.analchem.8b03837
24. Ahmed A, Tait SWG. Targeting immunogenic cell death in cancer. *Mol Oncol*. 2020;14(12):2994–3006. doi:10.1002/1878-0261.12851
25. Wolf NK, Kissiov DU, Raulet DH. Roles of natural killer cells in immunity to cancer, and applications to immunotherapy. *Nat Rev Immunol*. 2022;23(2):90–105. doi:10.1038/s41577-022-00732-1
26. Cachot A, Bilous M, Liu YC, et al. Tumor-specific cytolytic CD4 T cells mediate immunity against human cancer. *Sci Adv*. 2021;7(9):eabe3348. doi:10.1126/sciadv.abe3348
27. Talmadge JE, Gabrilovich DI. History of myeloid-derived suppressor cells. *Nat Rev Cancer*. 2013;13(10):739–752. doi:10.1038/nrc3581
28. Veglia F, Perego M, Gabrilovich D. Myeloid-derived suppressor cells coming of age. *Nat Immunol*. 2018;19(2):108–119. doi:10.1038/s41590-017-0022-x
29. Lewis SM, Williams A, Eisenbarth SC. Structure and function of the immune system in the spleen. *Sci Immunol*. 2019;4(33):eaau6085. doi:10.1126/sciimmunol.aau6085

International Journal of Nanomedicine

Dovepress

Publish your work in this journal

The International Journal of Nanomedicine is an international, peer-reviewed journal focusing on the application of nanotechnology in diagnostics, therapeutics, and drug delivery systems throughout the biomedical field. This journal is indexed on PubMed Central, MedLine, CAS, SciSearch[®], Current Contents[®]/Clinical Medicine, Journal Citation Reports/Science Edition, EMBase, Scopus and the Elsevier Bibliographic databases. The manuscript management system is completely online and includes a very quick and fair peer-review system, which is all easy to use. Visit <http://www.dovepress.com/testimonials.php> to read real quotes from published authors.

Submit your manuscript here: <https://www.dovepress.com/international-journal-of-nanomedicine-journal>